ADVANCED ENERGY MATERIALS
www.advenergymat.de

High-Rate Polymeric Redox in MXene-Based Superlattice-Like Heterostructure for Ammonium Ion Storage

Chaofan Chen, Glenn Quek, Hongjun Liu, Lars Bannenberg, Ruipeng Li, Jaehoon Choi, Dingding Ren, Ricardo Javier Vázquez, Bart Boshuizen, Bjørn-Ove Fimland, Simon Fleischmann, Marnix Wagemaker, De-en Jiang, Guillermo Carlos Bazan,* and Xuehang Wang**

Achieving both high redox activity and rapid ion transport is a critical and pervasive challenge in electrochemical energy storage applications. This challenge is significantly magnified when using large-sized charge carriers, such as the sustainable ammonium ion (NH_4^+). A self-assembled MXene/n-type conjugated polyelectrolyte (CPE) superlattice-like heterostructure that enables redox-active, fast, and reversible ammonium storage is reported. The superlattice-like structure persists as the CPE:MXene ratio increases, accompanied by a linear increase in the interlayer spacing of MXene flakes and a greater overlap of CPEs. Concurrently, the redox activity per unit of CPE unexpectedly intensifies, a phenomenon that can be explained by the enhanced de-solvation of ammonium due to the increased volume of 3 Å-sized pores, as indicated by molecular dynamic simulations. At the maximum CPE mass loading (MXene:CPE ratio = 2:1), the heterostructure demonstrates the strongest polymeric redox activity with a high ammonium storage capacity of 126.1 C g^{-1} and a superior rate capability at 10 A g^{-1}. This work unveils an effective strategy for designing tunable superlattice-like heterostructures to enhance redox activity and achieve rapid charge transfer for ions beyond lithium.

1. Introduction

Electrochemical energy storage (EES) devices, including rechargeable batteries and capacitors, are in increasing demand due to integrating more renewable energy sources into the grid and the growing adoption of electric vehicles.[1,2] Consequently, besides the imperative of enhancing performance, the significance of employing sustainable materials and green processes in the battery industry has escalated with the perspective of mitigating ecological implications.[3] Lithium-ion batteries dominate the EES industry due to their high energy density and relatively long cycling life. Sustainability concerns, however, have arisen due to the substantial consumption of lithium and specific transition metals, leading to resource depletion and increased raw materials costs.[4] Furthermore, the reliance on organic solvents

C. Chen, L. Bannenberg, B. Boshuizen, M. Wagemaker, X. Wang
Department of Radiation Science and Technology
Delft University of Technology
Delft 2629 JB, The Netherlands
E-mail: X.Wang-22@tudelft.nl

G. Quek, R. J. Vázquez, G. C. Bazan
Departments of Chemistry and Chemical & Biomolecular Engineering
National University of Singapore
Singapore 119077, Singapore
E-mail: chmbgc@nus.edu.sg

The ORCID identification number(s) for the author(s) of this article can be found under https://doi.org/10.1002/aenm.202402715

DOI: 10.1002/aenm.202402715

H. Liu, D.-en Jiang
Department of Chemical and Biomolecular Engineering
Vanderbilt University
Nashville, TN 37235, USA
E-mail: de-en.jiang@vanderbilt.edu

R. Li
National Synchrotron Light Source II
Brookhaven National Laboratory
Upton, NY 11973, USA

J. Choi, S. Fleischmann
Helmholtz Institute Ulm (HIU)
89081 Ulm, Germany

J. Choi, S. Fleischmann
Karlsruhe Institute of Technology (KIT)
76021 Karlsruhe, Germany

D. Ren, B.-O. Fimland
Department of Electronic Systems
Norwegian University of Science and Technology
Trondheim NO-7491, Norway

in electrolytes and during electrode fabrication processes leads to safety hazards and environmental risks.[5] Aqueous ammonium ion (NH_4^+) storage is an emerging sustainable EES option, given that its electrolyte comprises earth-abundant elements that are theoretically unlimited.[6] However, NH_4^+ as a charge carrier exhibits distinct EES characteristics compared to metal ions due to its nestled charge and tetrahedral structure. It interacts with electrodes through hydrogen bonds and exhibits preferred orientations.[7] Hydrogen bond formation may lead to smaller electrochemical polarization and faster kinetics when NH_4^+ ions are used as charge carriers in some transition metal-based layered materials (V_2O_5 and cobalt–nickel double hydroxide), compared to Na^+ or K^+ charge carriers.[8,9]

Common cathode materials for NH_4^+ storage include Prussian blue analogues (PBAs), vanadium-based oxides, and manganese-based compounds,[8,10,11] which typically possess flexible structures with spacious and adjustable internal voids. For instance, copper hexacyanoferrate (CuHCF), with its open hexacyanometalate framework, can undergo reversible NH_4^+ intercalation at 1.02 V (vs S.H.E.), accompanied by the conversion between Cu^{2+} and Cu^+, resulting in a specific capacity of 60 mAh g^{-1} at 50 mA g^{-1}.[10] The selection of anode materials is constrained by the need for low intercalation potential, with transition metal sulfides and organic materials being the typical choices.[12–14] Organic materials undergo reversible volumetric redox reactions concomitant with ammonium adsorption/desorption, thereby enabling a high NH_4^+ storage capacity.[7,13,15] For example, 3,4,9,10-perylenetetracarboxylic diimide demonstrated a capacity of 119 mAh g^{-1} and good cycling stability at low rates.[16] However, organic electrodes typically encounter diffusion-limited redox activities and structural degradation at high charging rates, further exacerbated when large-sized NH_4^+ charge carriers are used. Developing materials capable of sustaining robust redox activity and structural integrity at elevated rates with NH_4^+ is particularly important for aqueous systems.

A promising candidate for high-rate EES is the family of 2D early transition metal carbides and/or nitrides, known as MXenes. MXenes are characterized by a general formula of $M_{n+1}X_nT_x$ (n = 1–4), where M, X, and T_x represent the transition metal, carbon/nitrogen, and surface groups, respectively.[17] They stand out for their excellent high-rate performance and long cycling life in various electrolytes, attributed to their superior electronic conductivity and flexible interlayer spacing.[18–20] Additionally, the abundant surface groups of MXenes can facilitate rapid surface redox reactions with various intercalated ions, contributing to pseudocapacitive behavior.[21,22] MXene as an NH_4^+ host, demonstrates highly reversible NH_4^+ storage capability, albeit yielding a moderate capacitance of ≈ 50 F g^{-1}. This moderate capacitance is attributed to its weak surface interaction with NH_4^+ and reduced ion accessibility caused by the restacking of 2D MXene layers.[23] Constructing MXene/conductive polymer heterostructures represents an efficient strategy to enhance redox activity and alleviate restacking issues of MXenes. Simultaneously, MXene offers a conductive framework and confinement for polymer chains, thereby enhancing charge transfer and prolonging cycling life. This synergistic effect between MXene and a polymer has been successfully utilized to enhance proton storage capacity in sulfuric acid electrolytes.[24,25] For example, $Ti_3C_2T_x$ MXene/polypyrrole (PPy) composite, which was prepared by in situ polymerization of PPy in-between $Ti_3C_2T_x$ layers, showed a high capacitance and excellent cycling stability, up to 25 000 cycles.[25]

Evenly-spaced and interconnected MXene-based heterostructure with ordered 2D stacking can maximize the heterogeneous interface between MXenes and polymers, which is crucial for leveraging the synergistic effect. Such an ordered structure has demonstrated great promise in significantly enhancing the mechanical properties.[26] However, the formation of MXene-polymer composites often disrupts the ordered stacking of 2D MXenes, preventing the full exploitation of the benefits inherent in the heterogeneous structure. Moreover, MXene has been primarily composited with various p-type polymers, including, PPy, polyaniline,[27] and poly(3,4-ethylenedioxythiophene),[28] which require positive potentials to fully utilize their redox properties. On the other hand, MXene is susceptible to irreversible oxidation at positive potentials (ca. 0.2 V vs Ag) and is predominantly redox-active in the negative potential range (≈ −1.2 V to 0 V vs Ag in neutral aqueous electrolytes).[23,29] This limits the application of MXene/p-type polymer composites to the negative potential range, where the redox activity and pseudocapacitance contribution of p-type polymers are not fully accessible. This motivates the design of a novel MXene-polymer heterostructure with an ordered structure and a matched redox-active working window.

This work reports a superlattice-like MXene@conjugated polyelectrolyte (CPE) heterostructure, enabling high-rate and redox-active NH_4^+ EES storage. CPEs are characterized by conjugated polymer backbones appended with ionic side chains and have recently demonstrated high-rate pseudocapacitive performance for alkali ions.[30,31] For instance, a p-type CPE-K film can deliver a high rate performance of 67 F g^{-1} at 100 A g^{-1} as a positive electrode for K^+ storage, due to the presence of an ionic lattice in its ordered structure.[30] As an n-type CPE, p(cNDI-gT2) comprises alternating naphthalene-1,4,5,8-tetracarboxylic diimide (NDI) and 3,3′-dialkoxybithiophene structural units. The ammonium cationic functionalities on the side chain endow p(cNDI-gT2) with water solubility. Leveraging the excellent water solubility of $Ti_3C_2T_x$ and p(cNDI-gT2) CPE and their oppositely charged surfaces, we synthesized the Ti_3C_2@CPE heterostructures via a facile and green self-assembly process in water. In Ti_3C_2@CPE composites, CPEs are confined and realigned in the interlayer of $Ti_3C_2T_x$, increasing the interlayer spacing of MXene. The resulting Ti_3C_2@CPE composites showed a periodic layered stacking pattern perpendicular to the base plane of MXene, resembling a superlattice structure. Notably, with increased CPE:MXene ratio, the ordered layered structure was maintained with a linear expansion in the interlayer spacing, attributed to the gradual overlay of CPEs between MXene layers. Such a superlattice-like configuration enables heterostructures with effective charge transfer and improved structural stability. Unexpectedly, a higher CPE loading in the heterostructure

R. J. Vázquez
Department of Chemistry
Indiana University
Bloomington 47405-7102, USA

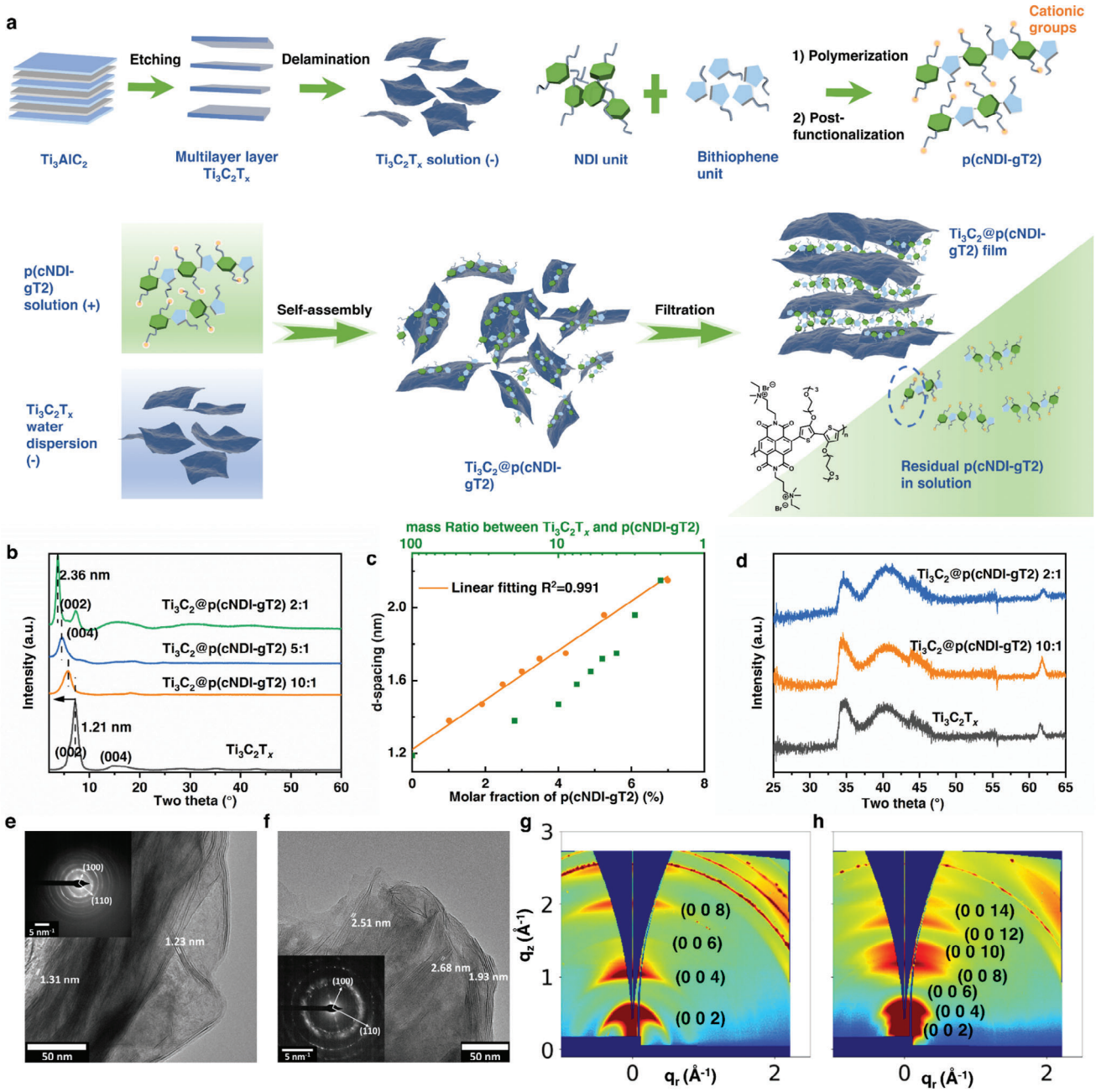

Figure 1. a) Schematic illustration of the synthesis process and self-assembly process of $Ti_3C_2T_x$ and p(cNDI-gT2) CPE. b) Bragg–Brentano XRD patterns of $Ti_3C_2T_x$ film and self-assembled Ti_3C_2@CPE film with different mass ratio (10:1, 5:1, and 2:1). c) The d-spacing change of Ti_3C_2@CPE with different MXene:CPE ratio. The orange dots represent the d-spacing of $Ti_3C_2T_x$ with different molar fractions of CPE, while the green dots show the corresponding mass ratio between $Ti_3C_2T_x$ and CPE. d) Transmission XRD patterns of $Ti_3C_2T_x$ and Ti_3C_2@CPE films. High-resolution transmission electron microscopy imaging of e) $Ti_3C_2T_x$ and f) Ti_3C_2@CPE 2:1, including selected area electron diffraction pattern as insets. Grazing incidence wide-angle X-ray scattering of g) $Ti_3C_2T_x$ film and h) Ti_3C_2@CPE 2:1.

enhances the polymeric redox (or polymer utilization) per unit of polymer. Hereby, the Ti_3C_2@CPE 2:1 electrode with the highest CPE loading delivered a high specific charge of 126.1 C g^{-1} at 0.1 A g^{-1} (1.5 times higher than that of $Ti_3C_2T_x$), and a superior rate capability (102.8 C g^{-1} at 10 A g^{-1}) in combination with a long cycling life (10 000 cycles) for NH_4^+ ion storage.

2. Results and Discussion

Figure 1a illustrates the preparation of p(cNDI-gT2) CPE and $Ti_3C_2T_x$ MXene, as well as the self-assembly process between the two components in water. CPEs are polymers characterized by conjugated backbones bearing ionic functionalities that enable synthetically tunable physico-electrochemical property.[31,32] We

chose p(cNDI-gT2) due to the following key structural features: 1) electron-accepting NDI units in the conjugated backbone confer the CPE a negative redox potential window (−0.9 to 0.3 V vs Ag/AgCl) matching that of the MXene; 2) cationic quaternary ammonium groups on the side chains facilitate water-processibility and electrostatic-driven self-assembly with negatively-charged MXene flakes; and 3) oligo(ethylene glycol) side chains further enhance water-processibility and ionic transport.[33] p(cNDI-gT2) was synthesized via direct arylation polymerization (DAP), followed by a post-functionalization step to install cationic groups on the side chains of the NDI unit.[33] Due to polar side chains, p(cNDI-gT2) can be well dispersed in water with a positive zeta potential of +61 mV (Figure S1, Supporting Information). $Ti_3C_2T_x$ was prepared by in situ HF etching from the Ti_3AlC_2 precursor, followed by sonication-assisted delamination (Figure 1a).[17] Due to the existence of the hydrophilic surface groups, MXene usually shows a zeta potential from −80 to −30 mV in water,[34] enabling it to be assembled with positively charged p(cNDI-gT2) CPE through complementary electrostatic interactions. The facile self-assembly of $Ti_3C_2T_x$ and CPE was performed by mixing $Ti_3C_2T_x$ and the p(cNDI-gT2) aqueous solution in various weight ratios (10:1, 5:1, and 2:1 of $Ti_3C_2T_x$-to-p(cNDI-gT2)). The resulting composites are denoted as Ti_3C_2@CPE r:1, where "r" signifies the weight ratio of $Ti_3C_2T_x$-to-p(cNDI-gT2). Upon the addition of CPE to the MXene solution, self-assembly takes place immediately (depicted in Figure 1a) as agglomeration was observed within a few seconds, yielding precipitates (Figure S2, Supporting Information). The maximum CPE loading that can be assembled with MXene is observed at an $Ti_3C_2T_x$:CPE ratio of 2:1. The agglomerates were obtained as flexible and self-freestanding films (Figure S3, Supporting Information) by vacuum-assisted filtration, followed by drying at room temperature under vacuum, while excessive CPE remained in the filtrate (as illustrated in Figure 1a).

Bragg-Brentano X-ray diffraction (XRD) was employed to gain insights into the structure of Ti_3C_2@CPE films. The XRD pattern of p(cNDI-gT2) in the powder form displays a diffraction peak at $2\theta = 5°$ (Figure S4, Supporting Information) that indicates interchain lamellar stacking, and a broad peak at $2\theta = 23°$ that corresponds to π-stacking of the conjugated backbones.[35] In contrast, the Ti_3C_2@CPE films only showed the signal of (0 0 *l*) diffraction peaks characteristic of $Ti_3C_2T_x$, indicating a preferential horizontal stacking. Compared to the pristine $Ti_3C_2T_x$ MXene, an obvious downshift of the (0 0 2) diffraction peak is observed for all three Ti_3C_2@CPE films, corresponding to increased *d*-spacings (Figure 1b). Specifically, the *d*-spacing of Ti_3C_2@CPE 10:1 and Ti_3C_2@CPE 5:1 film increased to 1.55 and 1.94 nm, respectively, while the Ti_3C_2@CPE 2:1 film showed an even larger *d*-spacing of 2.36 nm, which is nearly twice that of $Ti_3C_2T_x$ (1.21 nm). We attribute the increase in interlayer spacing to CPE pillared between $Ti_3C_2T_x$ sheets. Energy dispersive X-ray spectroscopy measurements (Figure S5, Supporting Information) reveal a homogeneous distribution of Ti, S, and N elements within the lamella Ti_3C_2@CPE structure, indicating that CPEs are uniformly sandwiched between adjacent $Ti_3C_2T_x$ layers.

The influence of the relative ratio of MXene-to-CPE in the composites on the interlayer spacing was systematically investigated by varying the mass ratios from 20:1 to 2:1 (Figure S6, Supporting Information). All films were dried at 150 °C under vacuum for 12 h before XRD inspection to remove the adsorbed water molecules between the layers as much as possible. Interestingly, the increase in *d*-spacing follows a linear correlation with the molar fraction of CPEs in the MXene-polymer composites (Figure 1c; Table S1, Supporting Information). This enables precise tuning of the interlayer spacing, while maintaining the regular layered patterns of MXene. Broadening of the (0 0 2) diffraction peak was observed in all Ti_3C_2@CPE films with ratios ranging from 20:1 to 3:1 (see Table S1, Supporting Information) compared to pristine MXene, indicating less uniform interlayer spacing. Surprisingly, a further increase in the loading of CPEs in a 2:1 composite resulted in the appearance of a sharp diffraction peak (Figure 1b), suggesting a highly uniform interlayer spacing.

Transmission XRD with the beam perpendicular to the film was employed on $Ti_3C_2T_x$, Ti_3C_2@CPE 10:1, and Ti_3C_2@CPE 2:1 to reveal possible structural features that may be buried under the intense (0 0 *l*) peaks or not shown in the Bragg–Brentano XRD patterns due to the significant preferential orientation of 2D MXene nanosheets (Figure 1d). For each film, there were low-intensity humps between $2\theta = 34°$ and 48°, which are attributed to the expected (0 1 *l*) diffractions of $Ti_3C_2T_x$ MXene.[36] No obvious difference between Ti_3C_2@CPE films and MXene has been observed. Analysis of the morphology and crystal structure of $Ti_3C_2T_x$ and Ti_3C_2@CPE was performed by transmission electron microscopy (TEM) (Figure 1e,f; Figure S7, Supporting Information). The 2D, flake-like morphology of $Ti_3C_2T_x$ is maintained after self-assembly with CPE for all ratios, as highlighted by the high-resolution TEM images. The interlayer spacing of each sample can be derived locally from HRTEM, showing consistency with XRD results by doubling from 1.2 - 1.3 nm for pure $Ti_3C_2T_x$ (Figure 1e) to 1.9 –2.7 nm for Ti_3C_2@CPE 2:1 (Figure 1f; Figure S8, Supporting Information). It should be noted that slight local variations in the interlayer spacings derived from HRTEM analysis, especially for polymer-functionalized samples, can be a consequence of the small crystalline domain sizes, i.e., few-layer character of the samples and potential electron beam damages during analysis. The crystal structure of the $Ti_3C_2T_x$ MXene sheets can further be locally analyzed using selected area electron diffraction (SAED). Strong diffraction rings can be observed at *d*-spacings of ca. 2.6 and 1.5 Å, corresponding to the (1 0 0) and (1 1 0) sets of planes of pristine $Ti_3C_2T_x$ MXene, respectively.[37] Furthermore, the absence of changes in diffraction ring position after polymer functionalization strongly indicates the absence of intralayer modification of MXene sheets by the self-assembly process, suggesting that CPE occupies exclusively interlayer space and does not incorporate into the $Ti_3C_2T_x$ crystal structure, for example, by forming covalent bonds.

More information on the orientational structure of the MXene@CPE films was obtained by performing 2D grazing incidence wide-angle X-ray scattering (GIWAXS) measurements. Generally, the shape of the Debye–Scherrer diffraction rings in GIWAXS data can provide insights into the overall crystallinity and texture. The width of the rings is associated with the size and distribution of crystallites, with peak broadening reflecting smaller crystallites, structural defects, or disorder. Additionally, the azimuthal angular distribution (χ) along the Debye-Scherrer rings sheds light on the orientation and ordering of crystallites, with anisotropic features indicating preferential alignment.[38] Consistent with the Bragg–Brentano XRD measurements and

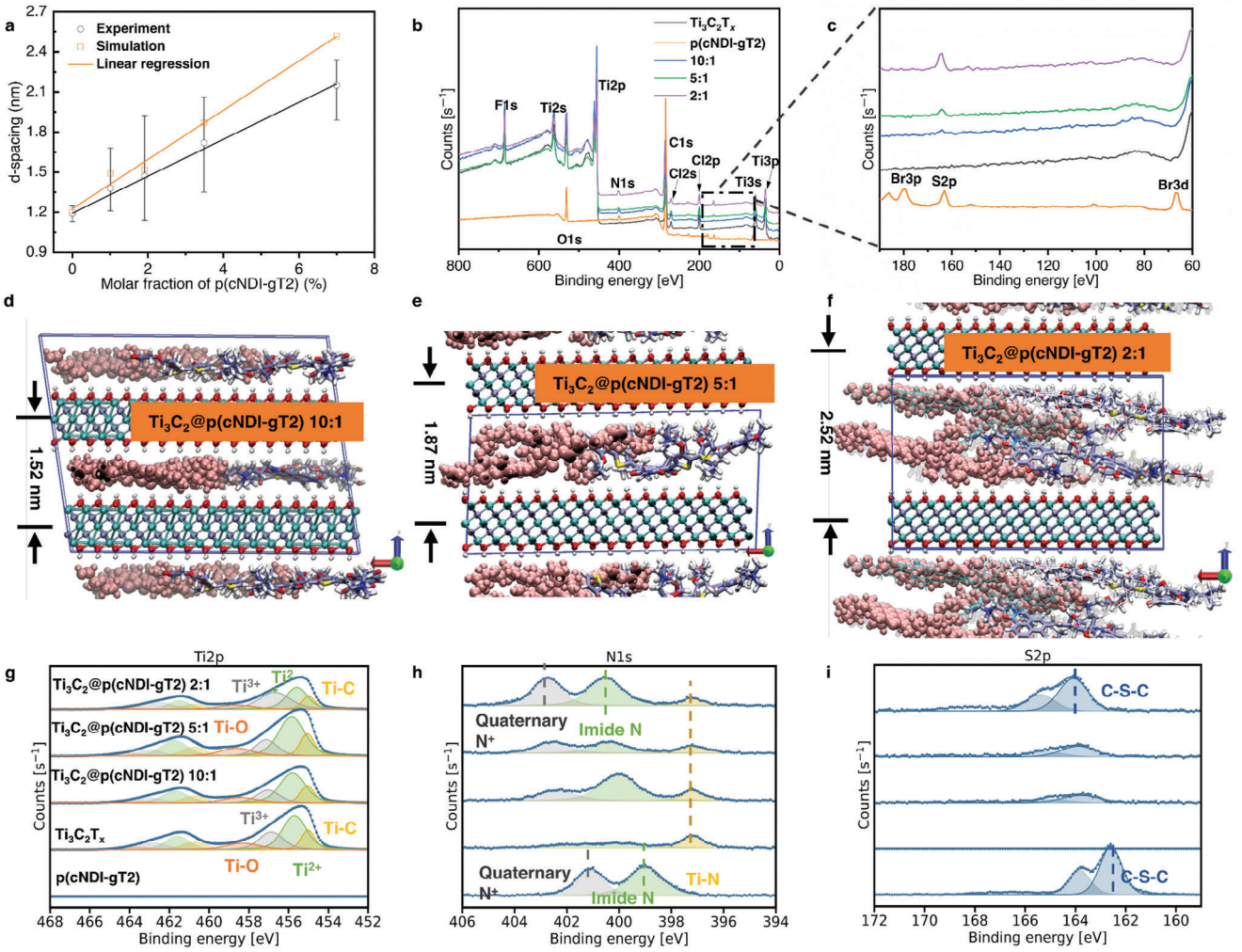

Figure 2. a) Comparison of d-spacings at different MXene:CPE molar fractions between experiments and molecular dynamics (MD) simulations. The error bar represents the d-spacing within the Full Width at Half Maximum (FWHM) region of the experimental result. b) XPS survey spectra of p(cNDI-gT2) CPE, $Ti_3C_2T_x$, Ti_3C_2@CPE. c) A magnification of the XPS survey spectra of p(cNDI-gT2), $Ti_3C_2T_x$, Ti_3C_2@CPE in selected binding energy region from 190 to 60 eV. d) Simulation snapshot of Ti_3C_2@CPE 10:1 showing the horizontal alignment of CPE between adjacent $Ti_3C_2T_x$ layers (the two different polymers are contrasted with the CPK model on the left and the stick model on the right). e) Simulation snapshot of Ti_3C_2@CPE 5:1 showing slightly inclined CPEs and their partial overlay in the middle of the unit cell, indicating an incipient bilayer. f) Simulation snapshot of Ti_3C_2@CPE 2:1 showing a bilayer stacking of slantly aligned CPEs with significant multilayer overlapping. g) High-resolution Ti2p X-ray photoelectron spectroscopy. h) High-resolution N1s X-ray photoelectron spectroscopy. i) High-resolution S2p X-ray photoelectron spectroscopy.

SAED, a preferred stacking of the MXene flakes along the c direction was observed for all Ti_3C_2@CPE. In $Ti_3C_2T_x$, four orders of the (0 0 *l*) direction were registered, corresponding to (0 0 2), (0 0 4), (0 0 6), and (0 0 8) planes, as shown in Figure 1g. Ti_3C_2@CPE 10:1 and Ti_3C_2@CPE 5:1 exhibited the same level of peak registration as $Ti_3C_2T_x$. However, much broader diffraction rings were observed in both Ti_3C_2@CPE 10:1 and Ti_3C_2@CPE 5:1 (Figure S9, Supporting Information). In the Ti_3C_2@CPE 2:1 film, six orders of the scattering peaks in (0 0 *l*) series were registered up to (0 0 14) reflection (Figure 1h). The missing (006) scattering is due to the minimum of the form factor of the materials. The scattering peaks of Ti_3C_2@CPE 2:1 film show narrower features in both q_z and azimuthal directions, compared to the 5:1, 10:1, and pristine $Ti_3C_2T_x$ films, suggesting a higher stacking order in the in-plane and out-of-plane directions.[26,39] This enhancement in stacking order indicates a superlattice-like structure where CPE is uniformly situated between $Ti_3C_2T_x$ layer, providing a periodic pattern.

Molecular dynamic (MD) simulations were carried out to reveal the structures of Ti_3C_2@CPE heterostructures at the atomistic level. As shown in **Figure 2a**, the simulated *d*-spacing displays a linear increase with the polymer concentration in the composite and is in reasonable agreement with the experimental values. To reveal the composite structure behind the increasing spacing with the polymer concentration, we analyzed typical snapshots from the MD simulations for the 10:1, 5:1, and 2:1 structures of the Ti_3C_2@CPE composites. As shown in Figure 2d for the 10:1 structure, the CPEs lie parallelly between the MXene layers, forming a neat monolayer with interlocking side chains (see Figure S10, Supporting Information, for a large top view).

As the CPE loading increases to MXene:CPE = 5:1 (Figure 2e), the CPEs are slightly inclined with noticeable crowding and overlapping (Figure S10, Supporting Information), increasing the d-spacing to 1.91 nm. Meanwhile, the enlarged interlayer spacing may allow the side chains of CPE moving more freely when they are not densely packed. Hence, we can observe the increased (0 0 2) peak width when the mass ratio of Ti_3C_2-to-CPE increases from 20:1 to 3:1 (Figure S6, Supporting Information). In contrast, the Ti_3C_2@CPE 2:1 heterostructure shows a pseudo-bilayer stacking pattern (Figure 2f), where the crowding CPEs are slantingly aligned in two layers with significant overlapping (Figure S10, Supporting Information). This leads to a narrower (0 0 2) peak width, indicating a narrow distribution of the interlayer space.

The successful assembly between $Ti_3C_2T_x$ and CPE was further confirmed by X-ray photoelectron spectroscopy (XPS). As illustrated in Figure 2b,c, no sulfur was detected in $Ti_3C_2T_x$, while the intensity of sulfur peak gradually increased with more CPE presenting in Ti_3C_2@CPE heterostructures. The interaction between polymers and MXenes may involve electrostatic attraction, hydrogen bonding, van der Waals interaction, π-π interaction, and/or covalent bonding, depending on the structure of the polymers.[24,40,41] As mentioned above, $Ti_3C_2T_x$ nanosheets show negative surface charge due to the electronegative functional groups. Meanwhile, the side chains of p(cNDI-gT2) CPE contain positively charged ammonium groups, which are balanced by bromide ions (Br^-) to obtain charge neutrality. After self-assembly, particularly relevant change in the XPS spectra is the absence of a Br signal for the Ti_3C_2@CPE composites, in contrast to pure p(cNDI-gT2) CPE (Figure 2c). Due to the robust electrostatic attraction between the cationic ammonium groups of CPE and the negatively charged surface of $Ti_3C_2T_x$, the removal of Br^- ions is necessary to maintain charge neutrality, aligning well with findings reported previously.[40] Hence, the depletion of Br^- in the heterostructures confirms that the electrostatic interactions contribute to the self-assembly process. More information about the chemical environment and the possible interaction in Ti_3C_2@CPE heterostructures were obtained by analyzing the high-resolution scans of Ti2p, N1s, S2p, O1s, C1s, Cl2p, and F1s spectra (Figure 2g–i; Figure S11, Supporting Information). Importantly, no covalent bonds were formed between $Ti_3C_2T_x$ and CPE, as shown by the high-resolution Ti2p XPS spectra. The Ti2p XPS spectrum of $Ti_3C_2T_x$ was fitted into four peaks at 454.9/460.6, 455.6/461.5, 456.7/462.6, and 458.2/463.6 eV (Ti2p3/2 / Ti2p1/2) corresponding to Ti-C, Ti(II), Ti(III), and Ti-O (Ti(IV)), respectively (Figure 2g).[42,43] No noticeable change in the Ti2p spectra can be seen after self-assembly, indicating the absence of covalent bonds between CPE and surface Ti atoms. Interestingly, all fitted XPS peaks that belong to CPE, irrespective of elements, showed significant blueshift (≈ 1.5 eV) in binding energy (BE) after self-assembly (Figure 2h,i; Figure S11, Supporting Information), even after we correct for the shift of the hydrocarbon peak at 284.8 eV in the C1s spectra (at max 0.2 eV shift). Such a shift in BE could arise from local sample charging and/or the presence of an electric field due to aligned dipole moments (More discussions see Figure S11, Supporting Information). Fourier transform infrared spectroscopy (FTIR) was also performed (Figure S12, Supporting Information), revealing a featureless FTIR spectrum for the $Ti_3C_2T_x$ film, consistent with previous reports.[40] Weak signals belonging to CPE were observed in Ti_3C_2@CPE 2:1, validating the existence of the polymer in the heterostructure.

To understand the relationship between the tunable structure of Ti_3C_2@CPE and its electrochemical NH_4^+ storage behavior, we performed electrochemical characterizations on Ti_3C_2@CPE 10:1, 5:1, and 2:1 electrodes using three-electrode cells with 1 M NH_4Cl aqueous electrolyte. **Figure 3a** illustrates the cyclic voltammograms (CV) of the $Ti_3C_2T_x$ MXene, p(cNDI-gT2) CPE, and Ti_3C_2@CPE electrodes. Rectangular CVs (Figure S14b, Supporting Information) with no visible redox peaks were observed for $Ti_3C_2T_x$ in 1 M NH_4Cl aqueous electrolyte, indicating a pseudocapacitive behavior. The galvanostatic charge and discharge (GCD) curve of $Ti_3C_2T_x$ shows a sloping feature, in good agreement with the CVs (Figure S17b, Supporting Information). This behavior is consistent with the previous report of NH_4^+ storage in $Ti_3C_2T_x$ MXene, which can be attributed to the NH_4^+ (de-)intercalation.[23] A capacitance of 81.5 F g^{-1} was obtained at 0.1 A g^{-1} based on the discharge curve of MXene. Meanwhile, the CVs of p(cNDI-gT2) (Figure S14a, Supporting Information) feature two reduction peaks at −0.52 V (peak 1) and −0.80 V (peak 2) vs Ag/AgCl (3.5 M KCl). When NDI units interact with cations, per NDI unit experiences two sequential one-electron reduction processes, forming a radical anion and a dianion, respectively (Figure S15, Supporting Information).[32,44] During the anodic scan, the two oxidation peaks merged and formed a broad oxidation peak at −0.1 V, indicating a large overpotential for the radical dianion formation/elimination. This two-electron transfer process of p(cNDI-gT2) CPE during charge and discharge leads to a high capacity of 211 C g^{-1} (≈ 192.0 F g^{-1}) at 0.1 A g^{-1}. However, with increasing scan rates, the intensity of redox peaks (or peak currents) decreased, and the electrochemical polarization became more severe (a peak separation above 1 V at 20 mV s^{-1}), indicative of sluggish kinetics.

In comparison, the CVs of Ti_3C_2@CPE films show characteristic pseudocapacitive features – quasi-rectangular with two redox peaks with a small peak separation (Figure 3a). Notably, the second pair of reductive/oxidative peaks (peak 2) for Ti_3C_2@CPE 10:1, 5:1, and 2:1 are located at −0.57 V/−0.66 V, −0.57 V/−0.66 V and −0.63 V/−0.71 V vs Ag/AgCl, respectively. These redox peaks inherited from p(cNDI-gT2) further confirm that the structure of CPE remains unaltered after the assembly process. Compared to CPE, much smaller peak separations of ≈ 0.1 V were observed for all Ti_3C_2@CPE films. The redox peaks are more pronounced for Ti_3C_2@CPE 2:1 compared to that for 10:1 and 5:1, owing to the higher mass loading of CPE in the heterostructure (Figure 3a). Importantly, the redox peaks were observed even at high scan rates of 500 mV s^{-1}, reflecting fast charge storage kinetics (Figure 3b). Cyclic voltammetry was also conducted in 1 M NH_4NO_3 (Figure S16, Supporting Information), showing CVs with redox peaks located at the same potentials as those observed in NH_4Cl. This consistency suggests that the redox reactions are due to the interaction between NH_4^+ and the heterostructure, with minimal influence from the anions on the electrochemical behavior. The redox peaks shown in the CVs collected in 1 M NH_4Cl correlate well with the GCD curves, in which two short plateaus at ca. −0.4 and ca. −0.7 V can be observed (Figure S17e, Supporting Information). The calculated specific capacitance at different current densities is plotted in Figure 3c.

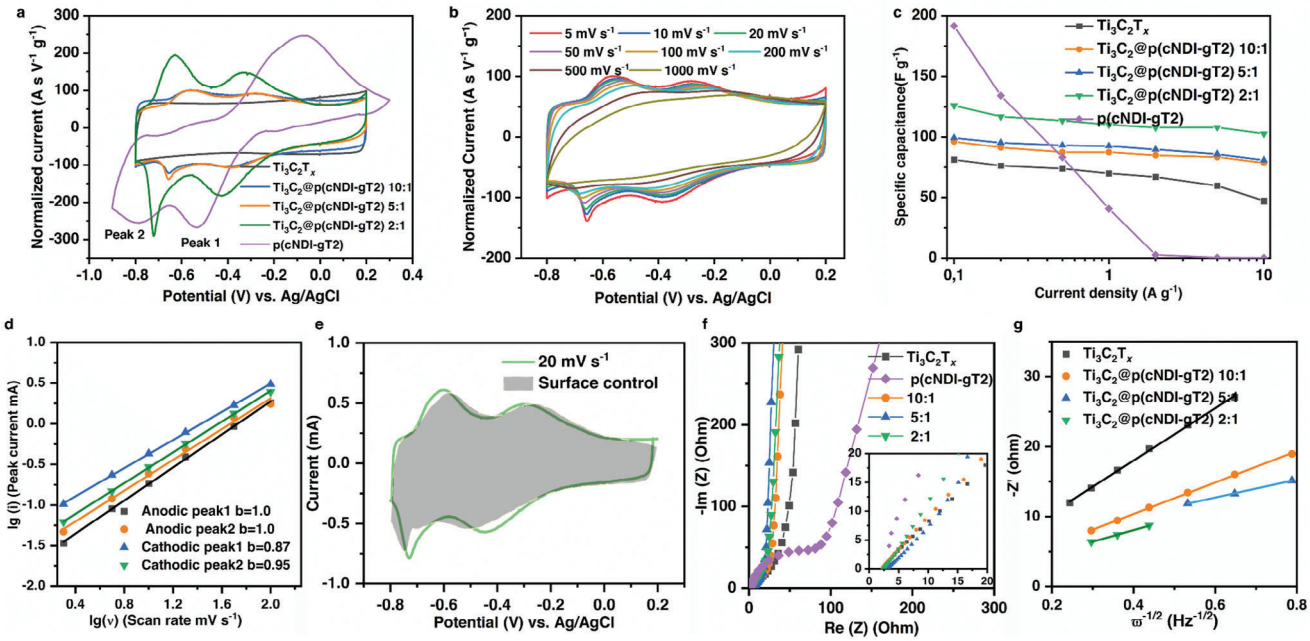

Figure 3. Electrochemical performance of $Ti_3C_2T_x$, p(cNDI-gT2) CPE and Ti_3C_2@CPE 2:1. CV curves of a) Comparison of CVs at 5 mV s^{-1}. b) CVs of Ti_3C_2@CPE 2:1 at different scan rates ranging from 5 mV s^{-1} to 1 V s^{-1}. c) Rate performance of $Ti_3C_2T_x$, p(cNDI-gT2) CPE and Ti_3C_2@CPE in 1 M NH_4Cl based on GCD. d) The relationship between cathodic and anodic peak currents and scan rates for Ti_3C_2@CPE 2:1. e) Pseudocapacitive contribution of Ti_3C_2@CPE 2:1 at 20 mV s^{-1}. f) Nyquist plots of $Ti_3C_2T_x$, p(cNDI-gT2), and Ti_3C_2@CPE films, where the inset shows a magnification of the high-frequency range. g) Linear fit showing the relationship between the real impedance (Z') and $\omega^{-1/2}$ of $Ti_3C_2T_x$ and Ti_3C_2@CPE in the Warburg frequency region.

Ti_3C_2@CPE 10:1, 5:1, and 2:1 show specific capacitances of 96.3 (96.3), 99.4 (99.4), and 126.1 C g^{-1} (126.1 F g^{-1}) at 0.1 A g^{-1}, respectively. These values are higher than that of MXene and can be attributed to additional capacity contributions from the redox-active CPE. Although p(cNDI-gT2) CPE alone showed the highest specific capacity at a low rate (0.1 A g^{-1}), its performance dropped drastically to 45.1 C g^{-1} (≈ 40.7 F g^{-1}) at 1 A g^{-1} and almost no capacity was delivered at 10 A g^{-1} (Figure S17a, Supporting Information). On the other hand, $Ti_3C_2T_x$ demonstrates a good rate capability, exhibiting a capacitance of 47.4 C g^{-1} (47.4 F g^{-1}, 58% retention) at 10 A g^{-1} (Figure S17b, Supporting Information). Remarkably, Ti_3C_2@CPE heterostructures delivered significantly improved rate performance over the individual components on their own, demonstrating a synergistic effect. This can be seen from the GCD curves at the high current density of 10 A g^{-1} as shown in Figure S17f (Supporting Information), where Ti_3C_2@CPE 2:1 delivered the longest discharge time among all the electrodes. Moreover, high capacitance retentions of 81.9% (78.9), 81.3% (80.9), and 81.5% (102.8 F g^{-1}) at 10 A g^{-1} was obtained for Ti_3C_2@CPE 10:1, 5:1, and 2:1, respectively. To gain a comprehensive understanding of the superior rate performance of Ti_3C_2@CPE for NH_4^+ storage, their charge storage kinetics are investigated. CVs collected at different scan rates were analyzed to determine the rate-limiting factor. The peak currents of CV curves and scan rates follow the power-law relationship:

$$i\ (V) = av^b \tag{1}$$

where i stands for the peak current, v represents the scan rate, a is a variable, and b is a parameter that determines the kinetics, ranging from 0.5 to 1.0. Typically, a diffusion-controlled process has a b value equal to 0.5, while an electrochemical process with $b = 1$ is dominated by surface-controlled behavior.[45] The b values for CPE were determined to be 0.75 for the first cathodic peak and 0.53 for the second cathodic peak (Figure S18, Supporting Information). The NH_4^+ storage on CPE is dominated by sluggish diffusion-controlled processes. In contrast, b values close to 1.0 were obtained for all Ti_3C_2@CPE electrodes (Figure 3d, Figure S19, Supporting Information), indicative of charge storage processes that are dominated by surface redox reactions. For instance, Ti_3C_2@CPE 2:1 electrode showed b values of 1.0 for both anodic peaks, and b values of 0.87 and 0.95 for the first and the second cathodic peaks, respectively (Figure 3d). The contribution of surface-controlled capacitance of Ti_3C_2@CPE 2:1 was further evaluated using the following equation:

$$i\ = k_1\ v + k_2 v^{1/2} \tag{2}$$

where v represents the scan rate, and k_1 and k_2 stand for the contribution of surface-controlled current and diffusion-controlled current, respectively.[46] Interestingly, 99% of the charge storage capacity for Ti_3C_2@CPE 2:1 is controlled by surface redox reaction (Figure 3e). This all-pseudocapacitive behavior indicates fast charge storage kinetics in the Ti_3C_2@CPE films.

Electrochemical impedance spectroscopy (EIS) measurements were carried out to further examine the kinetics of Ti_3C_2@CPE electrodes (Figure 3f) and fitted using the equivalent electric circuit (Figure S20 and Table S2, Supporting Information). The Nyquist plot of CPE shows a large semi-circle at high frequency, representing a large charge transfer resistance (≈ 65 Ω) for NH_4^+

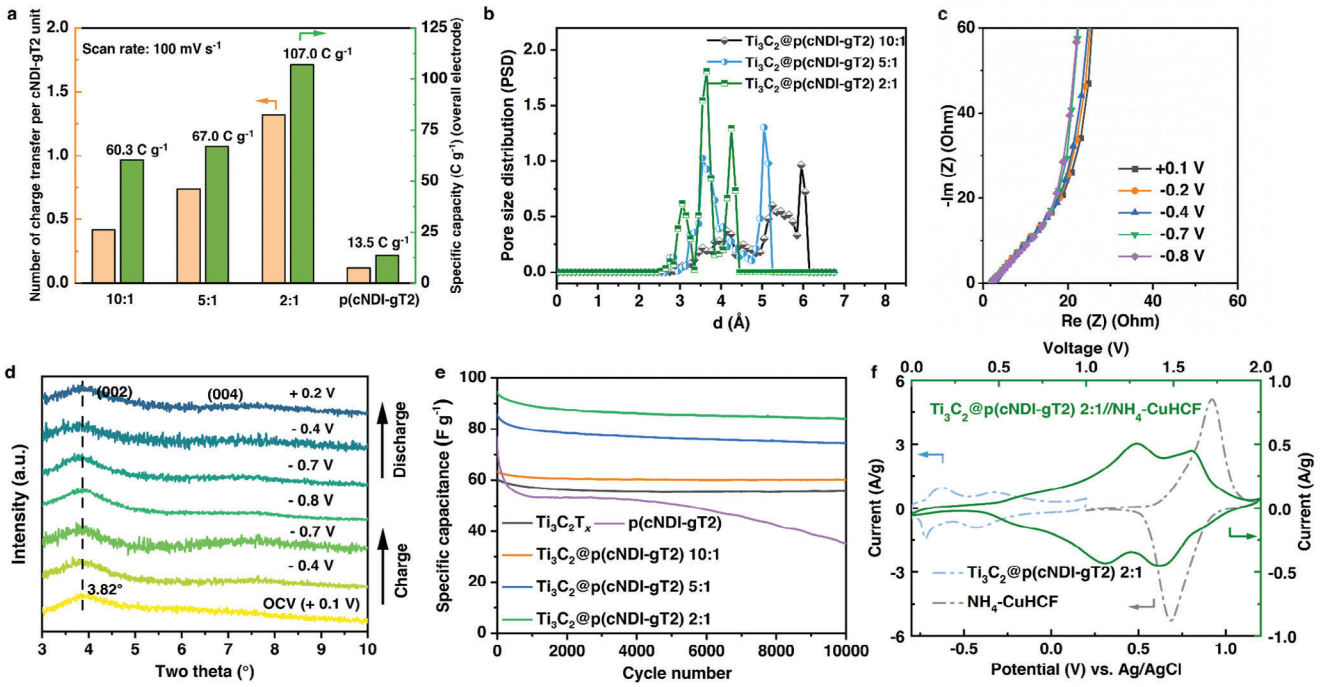

Figure 4. a) Charge transfer number of p(cNDI-gT2) CPE in different Ti_3C_2@CPE electrodes at 100 mV s^{-1}. b) Simulated pore size distribution of Ti_3C_2@CPE. c) Nyquist plots of Ti_3C_2@CPE 2:1 upon cathodic scan. d) Ex-situ XRD patterns of Ti_3C_2@CPE 2:1 electrode at different potentials. e) Cycling performance of $Ti_3C_2T_x$, p(cNDI-gT2) and Ti_3C_2@CPE at 1 A g^{-1}. f) CV curves of Ti_3C_2@CPE 2:1// NH_4-CuHCF hybrid capacitor.

storage. Compared to CPE, no evident semi-circles were observed for Ti_3C_2@CPE electrodes at high frequency, indicating negligible interfacial charge transfer resistance (lower than 1 Ω). This can be attributed to the reduced electron transfer resistance in the heterostructure. Additionally, the charge transfer process must overcome an activation barrier for ions to enter the hosting material.[47] Hence, the minimal charge transfer resistance also implies that solvated NH_4^+ ions are capable of being stored within the heterostructure. Besides, all Ti_3C_2@CPE electrodes exhibited a slope close to 90° at the low-frequency range, indicating typical capacitive behavior. Moreover, the Warburg factor (σ), or the slope of the linear fit of the real part of impedance vs $\omega^{-1/2}$ within the Warburg region (Figure S21, Supporting Information), was calculated to evaluate the kinetics of ion diffusion (Figure 3g). Ti_3C_2@CPE 5:1 shows the lowest slope (σ = 12) among all electrodes, which is then followed by Ti_3C_2@CPE 2:1 (σ = 16) and Ti_3C_2@CPE 10:1 (σ = 21) and $Ti_3C_2T_x$ (σ = 37). As the diffusion coefficient of ions is inversely proportional to the Warburg factor, a lower slope indicates faster ion diffusion in Ti_3C_2@CPE heterostructures, in contrast to the pristine $Ti_3C_2T_x$ electrode, due to the enlarged interlayer spacing. Importantly, the ionic diffusion coefficient of Ti_3C_2@CPE 2:1 is comparable to that of Ti_3C_2@CPE 5:1 structure. It implies that Ti_3C_2@CPE 2:1 film is capable of effective ion transport even with the close pseudo-bilayer stacking of CPE.

To understand the contribution of polymeric redox to the overall charge storage capacity, we evaluated the utilization of CPE (or electron transfer per structural unit) at different scan rates (from 5 to 100 mV s^{-1}) by analyzing CV curves (Table S3, Supporting Information). At high scan rates, all composites showed improved utilization of the CPE for charge storage relative to p(cNDI-gT2) CPE on its own, demonstrating the advantage of the self-assembled heterostructures for rapid charge storage kinetics. At 100 mV s^{-1}, the electron transfer number delivered per CPE unit of pristine CPE is only 0.12 (6% utilization). The number increases to 0.42 (21% utilization) and 0.74 (37% utilization) for Ti_3C_2@CPE 10:1 and 5:1, respectively. Interestingly, Ti_3C_2@CPE 2:1 exhibits the highest utilization of the CPE among all Ti_3C_2@CPE at all scan rates, with a charge transfer number of 1.32 (66% utilization) at 100 mV s^{-1} (**Figure** 4a; Table S3, Supporting Information). The crowded pseudo-bilayer stacking of CPE in the interlayer spacing of $Ti_3C_2T_x$ in Ti_3C_2@CPE 2:1 may lead to reduced NH_4^+ accessibility. Additionally, Ti_3C_2@CPE 2:1 shows slightly lower kinetics than Ti_3C_2@CPE 5:1, as previously discussed. However, Ti_3C_2@CPE 2:1 structure, which was expected to exhibit a lower electron transfer number (or utilization) compared to Ti_3C_2@CPE 5:1, actually demonstrates a higher electron transfer number. Such an anomalous increase in the polymer utilization in Ti_3C_2@CPE 2:1 structure is probably attributed to more effective charge transfer induced by NH_4^+ desolvation.[48] To confirm our assumption, the pore size distribution of each Ti_3C_2@CPE structure was evaluated based on the configurations from the MD simulations (Figure 4b). One can see that Ti_3C_2@CPE 2:1 shows a much higher distribution of smaller pores whose radius are comparable to bare NH_4^+ ions (≈ 3.0 Å in diameter, Figure 4b), which can enforce the striping of solvents due to the porous confinement effect.[49,50] The reinforced de-solvation can improve the interaction between NH_4^+ and CPE, and thereby results in more effective charge transfer.

Since Ti_3C_2@CPE 2:1 outperformed all other electrodes, its structural evolution and reaction kinetics during the charging process were further analyzed. A nearly vertical slope was

observed in the low-frequency region of Nyquist plots at all applied potentials during the intercalation of NH_4^+ for Ti_3C_2@CPE 2:1 (Figure 4c), which also confirmed the fast surface redox reaction upon NH_4^+ intercalation.[51] Ex situ XRD was conducted to monitor the structural evolution of Ti_3C_2@CPE 2:1 electrode upon NH_4^+ intercalation at different potentials. The (0 0 2) peak of Ti_3C_2@CPE 2:1 is maintained at 3.82° for all states of charge, indicating a constant *d*-spacing with NH_4^+ intercalation (Figure 4d). This negligible volume change of the electrode is beneficial for maintaining the structural integrity of the electrode, enabling high cycling stability. Remarkably, over 89% of the capacitance was retained after 10 000 cycles at a current density of 1 A g^{-1} for Ti_3C_2@CPE 2:1 (Figure 4e). Meanwhile, CPE on its own showed a lower capacitance retention of 46%, presumably due to its gradual dissolution into the aqueous electrolyte. As shown in Figure S22 (Supporting Information), after cycling p(cNDI-gT2) CPE in the NH_4Cl electrolyte, the glass fiber separator turned green, which indicates the dissolution of CPE in the electrolyte. In contrast, no color change of the separator was observed with Ti_3C_2@CPE 2:1 electrode, highlighting the superior structural stability of the Ti_3C_2@CPE heterostructure. The electrochemical test was also conducted in 1 M KCl electrolyte to showcase the benefits of Ti_3C_2@CPE 2:1 heterostructure (Figure S23, Supporting Information). A high capacitance of 123 F g^{-1} at 0.1 A g^{-1} and an impressive capacitance retention of 105 F g^{-1} at 10 A g^{-1} were achieved with 1 M KCl electrolytes, demonstrating the versatility of our superlattice-like structure for high-rate energy storage.

To demonstrate the potential of Ti_3C_2@CPE 2:1 electrode in a full cell, we fabricated an asymmetric hybrid capacitor based on a Ti_3C_2@CPE 2:1 negative electrode and anc $NH_4CuFe(CN)_6$ (NH_4-CuHCF) positive electrode. XRD and electrochemical performance of NH_4-CuHCF positive electrode are presented in Figures S24 and Figure S25 (Supporting Information). As shown in Figure 4f and Figure S26 (Supporting Information), Ti_3C_2@CPE 2:1//NH_4-CuHCF hybrid capacitor could be operated within a wide voltage window of 2.0 V in 1 M NH_4Cl. Two separate redox couples located at 1.1 V/1.3 V and 1.4 V/1.6 V were featured in CV and GCD, which is consistent with the two-step charging/discharging behavior of Ti_3C_2@CPE 2:1. Figure S27 (Supporting Information) illustrates the Ragone plots of the Ti_3C_2@CPE 2:1//NH_4-CuHCF hybrid capacitor and other state-of-the-art NH_4^+ storage devices based on polymer electrodes. An energy density of 14 Wh kg^{-1} at a power density of 2.2 kW kg^{-1} was achieved due to the outstanding rate performance of Ti_3C_2@CPE 2:1.

The Ti_3C_2@CPE superlattice structure constructed by self-assembly exhibited improved ammonium EES performance due to the maximized synergistic effect. First, the unique structure of Ti_3C_2@CPE enables polymeric redox contribution of the CPE, contributing to higher capacity. Second, the uniform stacking can maximize the heterogeneous interface between the highly conductive MXene and p(cNDI-gT2), ensuring fast electron transfer. Third, the p(cNDI-gT2) CPEs are situated between the MXene layer, expanding the interlayer spacing of MXene and suppressing tight self-restacking. This structure allows better NH_4^+ accessibility and fast ion diffusion, which leads to superior rate performance. Finally, the strong interfacial electrostatic interaction between MXene and the CPE helps improve the structural integrity of the electrode for maintaining long-term cycling stability. Importantly, the flexibility of fine-tuning this superlattice structure offers the chance to modify the microscopic structure of CPE within the interlayer of MXene while retaining the superlattice-like structure. Consequently, the polymeric redox activity was unexpectedly enhanced due to the increased volume of 3 Å-sized pores, which demonstrates the uniqueness of our Ti_3C_2@CPE heterostructure.

3. Conclusion

In this work, an n-type p(cNDI-gT2) CPE was self-assembled with $Ti_3C_2T_x$ MXene in water to construct Ti_3C_2@CPE superlattice-like structures for aqueous NH_4^+ storage. The green and facile self-assembly process is facilitated by cooperative interfacial electrostatic interactions between CPE and MXene flakes. In the Ti_3C_2@CPE heterostructure, CPE is sandwiched between adjacent MXene layers while MXene is able to maintain its ordered layered structure. The superlattice-like structure maximized the synergistic effects between CPE and MXene for NH_4^+ storage. The MXene component acts as an active material for NH_4^+ storage, provides a high electronic conductivity framework, prevents CPE dissolution, and constrains volume changes during cycling. The redox-active n-type CPE enhances NH_4^+ storage ability while acting as a spacer to enlarge interlayer spacing, supressing MXene restacking. Notably, the *d*-spacing of the MXene in the heterostructure could be adjusted by varying the amounts of CPE, while preserving the superlattice-like structure. With the highest polymer loading, Ti_3C_2@CPE 2:1 exhibited a significantly increased *d*-spacing of 2.36 nm compared to 1.15 nm in pristine $Ti_3C_2T_x$. The Ti_3C_2@CPE 2:1 sample also exhibited the highest utilization of CPE or the strongest polymeric redox of CPE. MD simulations suggest that the increased small pore volume, particularly in ≈ 3 Å-sized pores within Ti_3C_2@CPE 2:1, may facilitate the de-solvation of NH_4^+ ions and enhance redox activity. Consequently, Ti_3C_2@CPE 2:1 delivered a high specific charge storage capacity of 126.1 C g^{-1} at 0.1 A g^{-1} (1.5 times higher than that of $Ti_3C_2T_x$), superior rate capability of 81.5% retention at 10 A g^{-1} and high capacitance retention of 89% over 10 000 cycles for NH_4^+ storage. Further improvements in the capacitance of our heterostructure can be achieved by reducing the molecular weight of CPE and/or introducing additional redox-active sites, while maintaining the superlattice-like structure is essential to maximize the utilization of the new CPEs. Our results provide an efficient strategy for designing tunable superlattice-like structures and highlight the importance of fine-tuning the heterostructures to maximize the synergistic effects in the heterostructure for high-performance energy storage. This study also demonstrates a rational design routine for simultaneously facilitating redox activity and ion transport in the heterostructures, opening up new opportunities for a wide range of applications in energy conversion, harvesting, and storage.

4. Experimental Section

Synthesis of $Ti_3C_2T_x$: $Ti_3C_2T_x$ was prepared using conventional in situ HF etching method.[2] In general, 1 g of Ti_3AlC_2 was slowly added into the mixing etchant solution of 1.6 g LiF and 20 mL 9 M HCl and stirred

at 35 °C for 24 h in oil bath. The etched product was repeatedly washed with DI Water by centrifugation at 8 000 rpm until the PH of supernatant reached 6. Then, the sediment was re-dispersed in 40 mL DI water and sonicated for 1 h under argon to delaminate the multilayer. After that, the suspension was centrifuged at 3 500 rpm for 1 h and the supernatant was collected as few-layered $Ti_3C_2T_x$ colloidal solution. The concentration (≈ 8 mg mL^{-1}) of delaminated MXene solution was determined by vacuum-assisted filtration.

Synthesis of p(cNDI-gT2): p(cNDI-gT2) was synthesized according to a previous report – briefly, the neutral polymer p(NDI-gT2) was first prepared, followed by a post-functionalization step to install the cationic quaternary ammonium groups on the side chains.[33]

Self-Assembly of p(cNDI-gT2): The self-assembly of $Ti_3C_2T_x$ and p(cNDI-gT2) was manufactured by mixing $Ti_3C_2T_x$ MXene suspension (0.02 mg mL^{-1}) with (0.01 mg mL^{-1}) p(cNDI-gT2) solution in different weight ratio (10:1, 5:1, and 2:1) under vigorously stirring. The mixtures were then filtered with the assistance of vacuum. The excessive p(cNDI-gT2) was filtrated into the solution, while the assembled Ti_3C_2@p(cNDI-gT2) was washed with DI-water and formed a self-freestanding film after drying at RT.

Synthesis of NH_4-CuHCF: The NH_4-CuHCF was synthesized by a co-precipitation method as previously reported in the literature.[16] In general, 0.1 M $Cu(NO_3)_2$ (40 mL) was dropwise added into 40 mL 0.1 M $Na_4Fe(CN)_6$ solution under vigorous stirring. The $Na_2Cu[Fe(CN)_6]$ (Cu-HCF) precipitation was then collected and dried in the oven at 60 °C overnight. NH_4-CuHCF was prepared by the following ion-exchange method. Briefly, 1 g Cu-HCF was added into 40 mL of 1 M $(NH_4)_2SO_4$ solution and stirred for 6 h. After the exchange, the sediment was washed with DI water and dried in the oven for further characterization.

Electrochemical Measurements: The electrochemical performance of the Ti_3C_2@CPE in 1 M NH_4Cl was tested with a three-electrode configuration using Swagelok cells. Free-standing Ti_3C_2@CPE films were employed as the working electrode while Ag/AgCl (3.5 M) and activated carbon served as reference and counter electrode, respectively. The p(cNDI-gT2) electrode was obtained by coating the slurry of p(cNDI-gT2) powder, conductive acetylene black, and PVDF binder on the titanium foil current collector with a mass ratio of 8:1:1. The NH_4-CuHCF electrode was prepared by coating the slurry of NH_4-CuHCF powder, conductive acetylene black and PVDF binder on the aluminum foil in a mass ratio of 7:2:1.

All electrochemical measurements were performed using a Biologic VSP-300 potentiostat. Cyclic voltammetry was measured from 5 mV s^{-1} to 1 V s^{-1}. The current densities applied for galvanostatic charge and discharge (GCD) ranged from 0.1 to 10 A g^{-1}. Electrochemical impedance spectroscopy was recorded using a 10 mV amplitude with frequencies ranging from 10 mHz to 200 kHz.

The theoretical specific capacity of p(cNDI-gT2) was calculated according to:

$$q\left(\mathrm{C\,g^{-1}}\right) = \frac{nF}{M} \tag{3}$$

where n was the number of charge transfer, F was the Faraday constant (96 485 C mol^{-1}) and M was the molecular weight of polymer (g mol^{-1}).

The capacitance determined from CV was calculated according to:

$$C\ (\mathrm{F}) = \frac{\int i dv}{s\,\Delta V} \tag{4}$$

where i was the current (A), s (V s^{-1}) represented the scan rate and ΔV (V) was the applied voltage window.

The capacitance calculated from GCD (discharge branch) follows:

$$C\ (\mathrm{F}) = \int \frac{i dt}{dV} \tag{5}$$

In which V was the potential (V), i was the current (A) and t represented the discharge time (s).

Gravimetric specific capacitance C (F g^{-1}) was normalized by the mass of the working electrode.

For the full cell, the energy density was calculated by:

$$E\ (\mathrm{Wh\,kg^{-1}}) = \frac{\int V dq}{3.6\,m} \tag{6}$$

In which V was the potential (V), q was the charge (C) and m was the total mass of positive and negative electrode (g).

The power density was calculated by:

$$P\ \left(\mathrm{W\,kg^{-1}}\right) = \frac{3.6\,E}{\Delta t} \tag{7}$$

where E was the energy (Wh kg^{-1}) and Δt represented the discharge time (s).

MD Simulation: MD simulations were performed in BIOVIA Materials Studio suite. Mole ratio of surface termination groups was taken as F:O:OH = 1:1:1, according to the experimental value. Symmetric surface groups locate right above the central Ti in the FCC configuration. A $Ti_3C_2T_2$ orthorhombic supercell 4 × 3 × 1 (a × b × c) with 12 formula units initially taken from a previous DFT calculation[52] was used as a building block for Ti_3C_2@p(cNDI-gT2) heterostructures. The number of polyelectrolytes assembled into the interlayer of MXene was predetermined by specific mole ratio. Mass ratios between MXene and p(cNDI-gT2) of 10:1, 5:1, and 2:1 correspond to mole ratios of $Ti_3C_2T_2$ unit formula and monomer of 48:1, 24:1, and 12:1, respectively. A 16 × 12 × 1 supercell was used for $Ti_3C_2T_2$. The experimental d-spacings were taken as initial c lattice values, where nothing was between the interlayer of pristine $Ti_3C_2T_2$. The mole ratio of $Ti_3C_2T_2$: Li^+3H_2O was taken to model the structure without p(cNDI-gT2). The Universal Force Field was used for both MXene $Ti_3C_2T_2$ and polyelectrolyte p(cNDI-gT2) with two monomers.[53] Partial charges were calculated using the QEq method. The deprotonation of surface OH groups was applied to balance positive charge of polyelectrolyte. The supercells of heterostructures, subjected to isostatic external pressure of 1 atm, were geometrically optimized with atom positions and cell parameters following a previous study.[54] The resulting structures were used as initial configurations in subsequent MD runs. NPT MD simulations were run at 298 K and 1 atm for 1 ns for equilibration and another 500 ps for production. The equilibrated trajectories were used for structural analysis. Pore size distribution with N_2 as the probe was calculated using PoreBlazer v4.0.[55]

Supporting Information

Supporting Information is available from the Wiley Online Library or from the author.

Acknowledgements

C.C., G.Q., and H.L. contributed equally to this work. Great appreciation to Professor Y. Gogotsi for his insightful suggestions and comments on the manuscript. Sincere gratitude to S. Ganapathy for her help with the SS NMR measurement, and B. Terpstra for the help with ICP measurement and analysis. Many thanks to X. Liu for the efforts in the Transmission XRD measurement. This work was supported by NWO open competition m (OCENW.M.22.303). This work was also supported by the National University of Singapore start-up grant R143-000-A97-133, the Research Centre of Excellence award to the Institute for Functional Intelligent Materials from the Singapore Ministry of Education (I-FIM, project No. EDUNC-33-18-279-V12), and the Office of Naval Research (ONR-Global, N62909-22-1-2016). G.Q. acknowledges funding from the President's Graduate Fellowship (PGF) under the National University of Singapore. D.J. was supported by the U.S. National Science Foundation under grant number CHE-2318105 (M-STAR CCI). This research used the 11-BM CMS beamline of the National Synchrotron Light Source II, a U.S. Department of

Energy (DOE) Office of Science User Facility operated for the DOE Office of Science by Brookhaven National Laboratory under Contract No. DE-SC0012704. S.F. and J.C. acknowledge funding from the German Federal Ministry of Education and Research (BMBF) in the "NanoMatFutur" program (grant No. 03XP0423) and basic funding from the Helmholtz Association. The FTIR measurements at NTNU were sponsored by the Research Council of Norway through the FRINATEK Program (Grant No. 302923).

Conflict of Interest

The authors declare no conflict of interest.

Data Availability Statement

The data that support the findings of this study are available from the corresponding author upon reasonable request.

Keywords

conjugated polyelectrolytes, heterostructure, interlayer spacing, MXene, NH_4^+ storage, self-assembly, superlattice

Received: June 21, 2024
Revised: August 7, 2024
Published online:

[1] P. Simon, Y. Gogotsi, *Nat. Mater.* **2020**, *19*, 1151.
[2] M. Li, J. Lu, Z. Chen, K. Amine, *Adv. Mater.* **2018**, *30*, 1800561.
[3] J. Li, J. Fleetwood, W. B. Hawley, W. Kays, *Chem. Rev.* **2022**, *122*, 903.
[4] R. Schmuch, R. Wagner, G. Hörpel, T. Placke, M. Winter, *Nat. Energy* **2018**, *3*, 267.
[5] A. Kwade, W. Haselrieder, R. Leithoff, A. Modlinger, F. Dietrich, K. Droeder, *Nat. Energy* **2018**, *3*, 290.
[6] J. Han, A. Varzi, S. Passerini, *Angew. Chem. Int. Ed.* **2022**, *61*, 202115046.
[7] Y. Sun, B. Yin, J. Yang, Y. Ding, M. Li, H. Li, J. Li, B. Jia, S. Zhang, T. Ma, *Energy Environ. Sci.* **2023**, *16*, 5568.
[8] C. Liu, M. Li, J. Meng, P. Hei, J. Wang, Y. Song, X.-X. Liu, *Adv. Funct. Mater.* **2024**, *34*, 2310437.
[9] S. Dong, W. Shin, H. Jiang, X. Wu, Z. Li, J. Holoubek, W. F. Stickle, B. Key, C. Liu, J. Lu, P. A. Greaney, X. Zhang, X. Ji, *Chem* **2019**, *5*, 1537.
[10] C. D. Wessells, S. V. Peddada, M. T. McDowell, R. A. Huggins, Y. Cui, *J. Electrochem. Soc.* **2011**, *159*, A98.
[11] Q. Chen, M. Song, X. Zhang, J. Zhang, G. Hou, Y. Tang, *J. Mater. Chem. A* **2022**, *10*, 15614.
[12] L. Han, J. Luo, R. Zhang, W. Gong, L. Chen, F. Liu, Y. Ling, Y. Dong, Z. Yong, Y. Zhang, L. Wei, X. Zhang, Q. Zhang, Q. Li, *ACS Nano* **2022**, *16*, 14951.
[13] S. Zhang, K. Zhu, Y. Gao, D. Cao, *ACS Energy Lett.* **2023**, *8*, 889.
[14] R. Zheng, Y. Li, H. Yu, X. Zhang, D. Yang, L. Yan, Y. Li, J. Shu, B.-L. Su, *Angew. Chem., Int. Ed.* **2023**, *62*, 202301629.
[15] Z. Tian, V. S. Kale, Y. Wang, S. Kandambeth, J. Czaban-Jóźwiak, O. Shekhah, M. Eddaoudi, H. N. Alshareef, *J. Am. Chem. Soc.* **2021**, *143*, 19178.
[16] X. Wu, Y. Qi, J. J. Hong, Z. Li, A. S. Hernandez, X. Ji, *Angew. Chem.* **2017**, *129*, 13206.
[17] M. Naguib, V. N. Mochalin, M. W. Barsoum, Y. Gogotsi, *Adv. Mater.* **2014**, *26*, 992.
[18] X. Li, Z. Huang, C. E. Shuck, G. Liang, Y. Gogotsi, C. Zhi, *Nat. Rev. Chem.* **2022**, *6*, 389.
[19] X. Wang, T. S. Mathis, K. Li, Z. Lin, L. Vlcek, T. Torita, N. C. Osti, C. Hatter, P. Urbankowski, A. Sarycheva, M. Tyagi, E. Mamontov, P. Simon, Y. Gogotsi, *Nat. Energy* **2019**, *4*, 241.
[20] M. Ghidiu, M. R. Lukatskaya, M.-Q. Zhao, Y. Gogotsi, M. W. Barsoum, *Nature* **2014**, *516*, 78.
[21] Y. Li, H. Shao, Z. Lin, J. Lu, L. Liu, B. Duployer, P. O. Å. Persson, P. Eklund, L. Hultman, M. Li, K. Chen, X.-H. Zha, S. Du, P. Rozier, Z. Chai, E. Raymundo-Piñero, P.-L. Taberna, P. Simon, Q. Huang, *Nat. Mater.* **2020**, *19*, 894.
[22] M. R. Lukatskaya, *Adv. Energy Mater.* **2015**, *5*, 1500589.
[23] M. R. Lukatskaya, O. Mashtalir, C. E. Ren, Y. Dall'Agnese, P. Rozier, P. L. Taberna, M. Naguib, P. Simon, M. W. Barsoum, Y. Gogotsi, *Science* **2013**, *341*, 1502.
[24] W. Yang, B. Huang, L. Li, K. Zhang, Y. Li, J. Huang, X. Tang, T. Hu, K. Yuan, Y. Chen, *Small Methods* **2020**, *4*, 2000434.
[25] M. Boota, B. Anasori, C. Voigt, M.-Q. Zhao, M. W. Barsoum, Y. Gogotsi, *Adv. Mater.* **2016**, *28*, 1517.
[26] K. A. S. Usman, J. Zhang, D. Y. Hegh, A. O. Rashed, D. Jiang, P. A. Lynch, P. Mota-Santiago, K. L. Jarvis, S. Qin, E. L. Prime, M. Naebe, L. C. Henderson, J. M. Razal, *Adv. Mater. Interfaces* **2021**, *8*, 2002043.
[27] K. Li, X. Wang, S. Li, P. Urbankowski, J. Li, Y. Xu, Y. Gogotsi, *Small* **2020**, *16*, 1906851.
[28] G. S. Gund, J. H. Park, R. Harpalsinh, M. Kota, J. H. Shin, T. Kim, Y. Gogotsi, H. S. Park, *Joule* **2019**, *3*, 164.
[29] X. Wang, S.-M. Bak, M. Han, C. E. Shuck, C. McHugh, K. Li, J. Li, J. Tang, Y. Gogotsi, *ACS Energy Lett.* **2022**, *7*, 30.
[30] B. R. P. Yip, R. J. Vázquez, Y. Jiang, S. R. McCuskey, G. Quek, D. Ohayon, X. Wang, G. C. Bazan, *Adv. Mater.* **2024**, *36*, 2308631.
[31] G. Quek, B. Roehrich, Y. Su, L. Sepunaru, G. C. Bazan, *Adv. Mater.* **2021**, *34*, 2203480.
[32] D. Moia, A. Giovannitti, A. A. Szumska, I. P. Maria, E. Rezasoltani, M. Sachs, M. Schnurr, P. R. F. Barnes, I. McCulloch, J. Nelson, *Energy Environ. Sci.* **2019**, *12*, 1349.
[33] G. Quek, R. J. Vázquez, S. R. McCuskey, B. Kundukad, G. C. Bazan, *Adv. Mater.* **2022**, *34*, 2203480.
[34] G. B. Tezel, K. Arole, D. E. Holta, M. Radovic, M. J. Green, *J. Colloid Interface Sci.* **2022**, *605*, 120.
[35] S. Sharma, N. B. Kolhe, V. Gupta, V. Bharti, A. Sharma, R. Datt, S. Chand, S. K. Asha, *Macromolecules* **2016**, *49*, 8113.
[36] M. Ghidiu, M. W. Barsoum, *J. Am. Ceram. Soc.* **2017**, *100*, 5395.
[37] M. Volkov, E. Willinger, D. A. Kuznetsov, C. R. Müller, A. Fedorov, P. Baum, *ACS Nano* **2021**, *15*, 14071.
[38] J. A. Steele, E. Solano, D. Hardy, D. Dayton, D. Ladd, K. White, P. Chen, J. Hou, H. Huang, R. A. Saha, L. Wang, F. Gao, J. Hofkens, M. B. J. Roeffaers, D. Chernyshov, M. F. Toney, *Adv. Energy Mater.* **2023**, *13*, 2300760.
[39] M. Boota, C. Chen, L. Yang, A. I. Kolesnikov, N. C. Osti, W. Porzio, L. Barba, J. Jiang, *Chem. Mater.* **2020**, *32*, 7884.
[40] M. Boota, M. Pasini, F. Galeotti, W. Porzio, M.-Q. Zhao, J. Halim, Y. Gogotsi, *Chem. Mater.* **2017**, *29*, 2731.
[41] X. Jin, W. Zhang, S. Liu, T. Zhang, Z. Song, W. Shao, R. Mao, M. Yao, X. Jian, F. Hu, *Chem. Eng. J.* **2023**, *451*, 138763.
[42] P. H. Nguyen, D. H. Nguyen, D. Kim, M. K. Kim, J. Jang, W. H. Sim, H. M. Jeong, G. Namkoong, M. S. Jeong, *ACS Appl. Mater. Interfaces* **2022**, *14*, 51487.
[43] R. B. Rakhi, B. Ahmed, M. N. Hedhili, D. H. Anjum, H. N. Alshareef, *Chem. Mater.* **2015**, *27*, 5314.
[44] C. R. DeBlase, K. Hernández-Burgos, J. M. Rotter, D. J. Fortman, D. dos S. Abreu, R. A. Timm, I. C. N. Diógenes, L. T. Kubota, H. D. Abruña, W. R. Dichtel, *Angew. Chem., Int. Ed.* **2015**, *54*, 13225.
[45] T. S. Mathis, N. Kurra, X. Wang, D. Pinto, P. Simon, Y. Gogotsi, *Adv. Energy Mater.* **2019**, *9*, 1902007.
[46] T. Brezesinski, J. Wang, J. Polleux, B. Dunn, S. H. Tolbert, *J. Am. Chem. Soc.* **2009**, *131*, 1802.
[47] S. Fleischmann, J. B. Mitchell, R. Wang, C. Zhan, D. Jiang, V. Presser, V. Augustyn, *Chem. Rev.* **2020**, *120*, 6738.
[48] K. Ge, H. Shao, E. Raymundo-Piñero, P.-L. Taberna, P. Simon, *Nat. Commun.* **2024**, *15*, 1935.

[49] J. Chmiola, G. Yushin, Y. Gogotsi, C. Portet, P. Simon, P. L. Taberna, *Science* **2006**, *313*, 1760.
[50] S. Fleischmann, Y. Zhang, X. Wang, P. T. Cummings, J. Wu, P. Simon, Y. Gogotsi, V. Presser, V. Augustyn, *Nat. Energy* **2022**, *7*, 222.
[51] X. Wang, T. S. Mathis, Y. Sun, W.-Y. Tsai, N. Shpigel, H. Shao, D. Zhang, K. Hantanasirisakul, F. Malchik, N. Balke, D. Jiang, P. Simon, Y. Gogotsi, *ACS Nano* **2021**, *15*, 15274.
[52] R. Peng, K. Han, K. Tang, *J. Electrochem. Soc.* **2022**, *169*, 060523.
[53] A. K. Rappe, C. J. Casewit, K. S. Colwell, W. A. Goddard, W. M. Skiff, *J. Am. Chem. Soc.* **1992**, *114*, 10024.
[54] O. Mashtalir, M. Naguib, V. N. Mochalin, Y. Dall'Agnese, M. Heon, M. W. Barsoum, Y. Gogotsi, *Nat. Commun.* **2013**, *4*, 1716.
[55] L. Sarkisov, R. Bueno-Perez, M. Sutharson, D. Fairen-Jimenez, *Chem. Mater.* **2020**, *32*, 9849.